# Intra- and intertrench variations in flexural bending of the Manila, Mariana and global trenches: implications on plate weakening in controlling trench dynamics

## Fan Zhang,[1,2,3,4] Jian Lin,[3,4] Zhiyuan Zhou,[4] Hongfeng Yang[5] and Wenhuan Zhan[4]

[1]*Department of Ocean Science and Engineering, Southern University of Science and Technology, Shenzhen 518055, China*
[2]*Key Laboratory of Computational Geodynamics, University of Chinese Academy of Sciences, Beijing 100081, China*
[3]*Department of Geology and Geophysics, Woods Hole Oceanographic Institution, Woods Hole, MA 02543, USA. E-mail: jlin@whoi.edu*
[4]*Key Laboratory of Ocean and Marginal Sea Geology, South China Sea Institute of Oceanology, Chinese Academy of Sciences, Guangzhou 510301, China. E-mail: zyzhou@scsio.ac.cn*
[5]*Earth System Science Programme, the Chinese University of Hong Kong, Shatin, Hong Kong*

## SUMMARY

We conducted detailed analyses of a global array of trenches, revealing systematic intra- and intertrench variations in plate bending characteristics. The intratrench variations of the Manila and Mariana Trenches were analysed in detail as end-member cases of the relatively young (16–36 Ma) and old (140–160 Ma) subducting plates, respectively. Meanwhile, the intertrench variability was investigated for a global array of additional trenches including the Philippine, Kuril, Japan, Izu-Bonin, Aleutian, Tonga-Kermadec, Middle America, Peru, Chile, Sumatra and Java Trenches. Results of the analysis show that the trench relief ($W_0$) and width ($X_0$) of all systems are controlled primarily by the faulting-reduced elastic thickness near the trench axis ($T_e^m$) and affected only slightly by the initial unfaulted thickness ($T_e^M$) of the incoming plate. The reduction in $T_e$ has caused significant deepening and narrowing of trench valleys. For the cases of relatively young or old plates, the plate age could be a dominant factor in controlling the trench bending shape, regardless the variations in axial loadings. Our calculations also show that the axial loading and stresses of old subducting plates can vary significantly along the trench axis. In contrast, the young subducting plates show much smaller values and variations in axial loading and stresses.

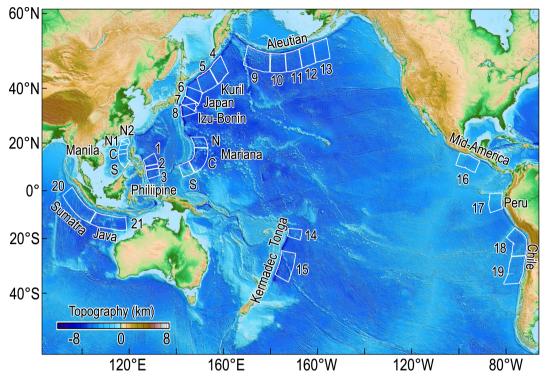**Key words:** Lithospheric flexure; Subduction zone processes.

## 1 INTRODUCTION

Near an ocean trench, the subducting plate bends due to tectonic loading, forming an axial trench valley and a bulge in the outer-rise region (e.g. Walcott 1970; Hanks 1971; Watts & Talwani 1974; McAdoo *et al.* 1978; Harris & Chapman 1994; Bry & White 2007). When the bending-induced stress exceeds the yield strength of the lithosphere, pervasive faulting could occur trenchward of the outer-rise region (e.g. Jones *et al.* 1978; Masson 1991; Ranero *et al.* 2003, 2005; Obana *et al.* 2012; Gou *et al.* 2013; Naliboff *et al.* 2013; Boston *et al.* 2014; Craig *et al.* 2014; Zhou *et al.* 2015). Faulting could in turn cause a significant reduction in the effective elastic thickness of the subducting plate (Turcotte *et al.* 1978; Bodine & Watts 1979; Watts 2001; Ranero *et al.* 2005; Contreras-Reyes & Osses 2010; Zhang *et al.* 2014; Hunter & Watts 2016). Thus, the flexural bending shape of a subducting plate contains important information on the tectonic loading at the trench axis, lithospheric strength and overall faulting effects of the subducting plate.

For a constant elastic plate, it was shown that the axial trench relief is negatively correlated to the effective elastic plate thickness

$T_e$, while the axial trench width is positively correlated to $T_e$ (e.g. Turcotte & Schubert 2014). However, such theoretical relationships are not applicable to the real cases of trenches, where $T_e$ is variable as a function of distance both across and along the trench axis. How the axial trench relief and width depend on the variability in $T_e$ of the subducting plate in reality is still poorly quantified.

A number of studies have quantified the effects of faulting in reducing the effective elastic thickness ($T_e$) of the subducting plate. Contreras-Reyes & Osses (2010) and Contreras-Reyes *et al.* (2013) showed that normal faulting has reduced the $T_e$ of the subducting plate of the Chile trench by 6–50 per cent. Zhang *et al.* (2014) showed that the $T_e$ for the Mariana Trench is reduced by 21–61 per cent due to trenchward faulting of the outer-rise region. Zhou *et al.* (2015) explicitly modeled normal faulting and elastoplastic deformation in a subducting plate and showed that normal faults could indeed reduce the $T_e$ significantly. Hunter & Watts (2016) showed that the $T_e$ for the circum-Pacific trenches is reduced by 20–72 per cent trenchward of the outer-rise region. Through admittance analysis of topography and gravity profiles of the Tonga-Kermadec and Japan-Izu-Bonin systems, Billen & Gurnis (2005) and Arredondo

**Figure 1.** Topographyof the global array of trenches. White boxes mark the profile locations of the Philippine (Sections 1–3), Kuril (Sections 4 and 5), Japan (Sections 6 and 7), Izu-Bonin (Section 8), Aleutian (Sections 9–13), Tonga-Kermadec (Sections 14 and 15), Middle America (Section 16), Peru (Section 17), Chile (Sections 18 and 19), Sumatra (Section 20) and Java (Section 21) trenches. Also shown are the locations of the analysed segments of the Manila (S, C, N1 and N2) and Mariana (S, C and N) Trenches.
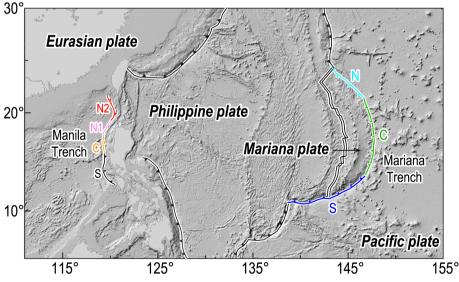


**Figure 2.** Topography map of the Manila, Mariana and several trenches in the Western Pacific Ocean (modified from Bird 2003). The Manila Trench is divided into the southern, central and northern N1 and N2 segments, while the Mariana Trench is divided into the southern, central and northern segments for analysis.

& Billen (2012) found that the flexural rigidity (*D*) and $T_e$ of the subducting plates decrease systematically from the outer-rise region to the trench axis. However, detailed analysis of along-trench variations in plate bending and $T_e$ is still relatively rare, and the interplay between reduction in the $T_e$ and trench dynamics is still poorly quantified.

In this study, we conducted detailed analyses of flexural bending at a global array of 13 trenches with a diverse range of characteristics. We first investigated, in relatively fine detail, the *intratrench* variations within two end-member examples of trenches: the rela-

tively young (15–36 Ma) Manila Trench and the relatively old (140–160 Ma) subducting plate at the Mariana Trench, respectively (Figs 1 and 2). For the Manila Trench, we conducted the first original analysis of this relatively young, shallow and narrow trench (Fig. C1). For the Mariana Trench, the detailed analyses were already accomplished by Zhang *et al.* (2014), and thus we only used the Mariana results in the synthesis of this study. We then investigated the *intertrench* variations by analysing a global array of 13 trenches, including the Manila, Mariana, Philippine, Kuril, Japan, Izu-Bonin, Aleutian, Tonga-Kermadec, Middle America, Peru, Chile, Sumatra

**Table 1.** Variables.

| Symbol | Variables | Value | Unit |
|---|---|---|---|
| $E$ | Young's modulus | $7 \times 10^{10}$ | Pa |
| $g$ | Acceleration due to gravity | 9.81 | m s$^{-2}$ |
| $\nu$ | Poisson's ratio | 0.25 | |
| $\rho_w$ | Sea water density | 1030 | kg m$^{-3}$ |
| $\rho_s$ | Sediment density | 2000 | kg m$^{-3}$ |
| $\rho_c$ | Crust density | 2700 | kg m$^{-3}$ |
| $\rho_m$ | Mantle density | 3300 | kg m$^{-3}$ |

and Java trenches (Fig. 1). Finally, we synthesized the results of both intra- and intertrench variations in terms of the mechanisms that control the trench dynamics.

Results of the analysis revealed that for all trenches, the trench depth and width are both controlled primarily by the faulting-reduced elastic thickness near the trench axis ($T_e^m$) and affected only slightly by the initial unfaulted thickness ($T_e^M$) of the incoming plate seaward of the outer-rise region. The reduction in the plate thickness has caused significant deepening and narrowing of the trench valley.

## 2 DATA ANALYSIS

### 2.1 Study regions

Topography, sediment thickness, gravity, crustal thickness, crustal age and other geophysical data were analysed, providing observational constraints on flexural bending models. The study regions include the Manila, Mariana and a global array of another 11 trenches. Analyses of all trenches were conducted using same methods.

*End-member example 1: Manila Trench*: the Manila Trench (Figs 1 and 2) is selected as an end-member example of a relatively young subducting plate (∼15–36 Ma, e.g. Briais *et al.* 1993; Li *et al.* 2014, 2015; Sibuet *et al.* 2016) with relatively small trench relief and width (Tables 2, and C1 and C2, Hayes & Lewis 1984; Rangin *et al.* 1999; Galgana *et al.* 2007; Lin 2015).

The Manila Trench can be divided roughly into four segments (Fig. 3).The southern (S) segment (13°–15.8°N) is associated with subducting oceanic crust (Fig. 2). The central (C) segment (15.8°–17.3°N) is also associated with subducting oceanic crust but contains numerous seamounts and fossil ridges. The northern zone is associated with subducting oceanic crust in segment N1 (17.3°–19.3°N), but subducting thinned continental crust in segment N2 (19.3°–21.1°N, Eakin *et al.* 2014). The northernmost of the Manila subduction system involves complex tectonics of arc–continent collision and double subduction zones (Yu 2000).

The bathymetry data of the Manila Trench were extracted from the version 18.1 of the global marine bathymetry database (Smith & Sandwell 1997, http://topex.ucsd.edu/WWW_html/mar_topo.html) with data grid spacing of 0.25 min (Fig. 3a). The axial depth of

the Manila Trench is 3.1–5.3 km (Figs 3a and 7a). The sediment thickness data of the Manila Trench (Fig. 3b) were extracted from the Atlas of Geology and Geophysics of the South China Sea (Yang *et al.* 2015) with data grid spacing of 2 min. The S and C segments of the Manila Trench are associated with a smaller range of sediment thickness variations (0.4–1.9 km) than the N1 and N2 segments (0.4–4.4 km).

*End-member example 2: Mariana Trench:* the Mariana Trench is selected as an end-member example of relatively old subducting plate (∼140–160 Ma, Müller *et al.* 2008) and relatively large trench relief and width (Tables 2, and C1 and C2, Zhang *et al.* 2014). The Mariana Trench is in the Western Pacific Ocean (Figs 1 and 2), where the Pacific plate is subducting under the Mariana microplate in the northern (N) and central (C) Mariana Trench but under the Philippine Sea plate in the southern (S) Mariana Trench. Data sources for the analysis of the Mariana Trench are described in detail in Zhang *et al.* (2014).

*A global array of trenches:* in addition to the Manila and Mariana Trenches, we also analysed another 11 trenches in the Pacific and Indian Oceans including the Philippine, Kuril, Japan, Izu-Bonin, Aleutian, Tonga-Kermadec, Middle America, Peru, Chile, Sumatra and Java trenches (Fig. 1). These trenches range in age of ∼20 to ∼160 Ma (Table 3; Müller *et al.* 2008), providing a broad spectrum of examples to investigate global variability and correlations.

The data source of the bathymetry used in the analysis of the Mariana and global array of trenches were similar to that of the Manila Trench. The sediment thickness data of the Mariana and global array of trenches were extracted from the version 2 of National Geophysical Data Center (NGDC) sediment database (Divins 2003; https://ngdc.noaa.gov/mgg/sedthick/) with grid spacing of 5 min. Results of the analysis of the Mariana Trench were given in Zhang *et al.* (2014), while the results of the global array of trenches were obtained in this study.

### 2.2 Observational constraints

We used the *interpreted plate deformation* as a proxy for plate flexural deformation, employing a set of modeling steps. The modeling approach is same for all trenches and is illustrated below using the example of the Manila Trench.
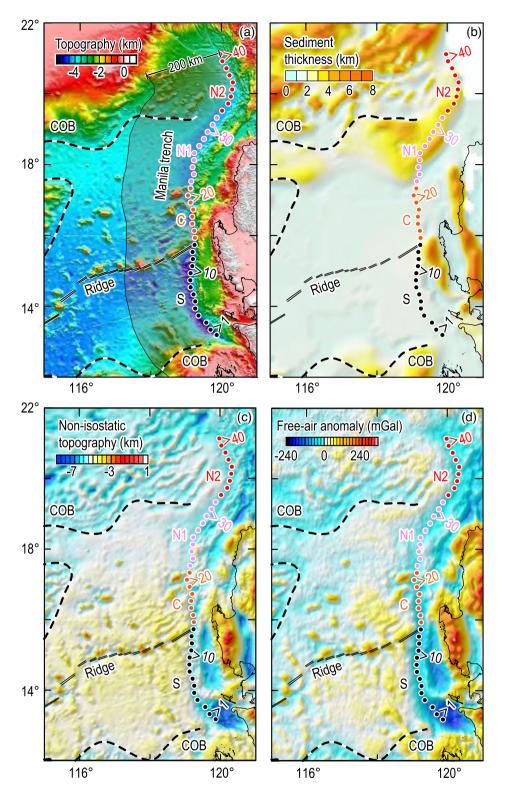
*Airy local isostatic topography:* we first calculated the expected Airy local isostatic topography due to spatial variations in sediment loading and crustal thickness. The Airy local isostatic topography ($T_{iso}$) is calculated by:

$$T_{iso} = H_{sed} \times \frac{(\rho_m - \rho_s)}{(\rho_m - \rho_w)} + (H_c - \overline{H_c}) \times \frac{(\rho_m - \rho_c)}{(\rho_m - \rho_w)}, \quad (1)$$

where $H_{sed}$ is sediment thickness; $H_c$ is gravity-derived crustal thickness (see Appendix A, Parker 1973; Kuo & Forsyth 1988) calibrated with seismic data (Qiu *et al.* 2001; Yan *et al.* 2001; Hayes & Nissen

**Table 2.** Best-fitting bending parameters of the Manila and Mariana segments.

| | Latitude (°) | $W_0$ (km) | $W_b$ (km) | $X_0$ (km) | $X_r$ (km) | $-V_0$ ($10^{12}$ N m$^{-1}$) | $M_0$ ($10^{16}$ N) | $T_e^m$ (km) | $T_e^M$ (km) | $T_e$ reduction (%) |
|---|---|---|---|---|---|---|---|---|---|---|
| S. Manila | 13.0/15.7 | 1.0/2.0 | 0.03/0.07 | 17/46 | 20/50 | 0.08/0.38 | 0/0.7 | 5/7 | 14/20 | 50/75 |
| C. Manila | 15.7/17.3 | 0.6/2.1 | 0.02/0.10 | 22/54 | 20/80 | 0.15/0.43 | 0/0.7 | 5/11 | 14/18 | 40/65 |
| N1. Manila | 17.3/19.3 | 0.4/0.8 | 0.04/0.07 | 35/66 | 15/80 | 0.03/0.28 | 0/0.6 | 9/14 | 14/18 | 25/35 |
| N2. Manila | 19.3/21.1 | 0.6/0.7 | 0.04/0.06 | 35/43 | 35/60 | 0.10/0.2 | 0.1/0.4 | 8/10 | 14/18 | 30/50 |
| S. Mariana | 11.2/13.7 | 1.7/5.7 | 0.12/0.65 | 42/105 | 70/100 | −0.20/3.17 | 1.0/27 | 19/32 | 45/50 | 32/61 |
| C. Mariana | 13.7/21.6 | 1.5/3.8 | 0.09/0.49 | 57/96 | 60/125 | −0.55/1.66 | 1.3/26 | 21/37 | 46/52 | 26/61 |
| N. Mariana | 21.6/23.6 | 0.9/2.2 | 0.19/0.35 | 51/87 | 80/90 | −0.73/0.70 | 10/20 | 30/40 | 48/50 | 21/39 |

**Figure 3.** (a) Seafloor bathymetry of the Manila Trench and surrounding regions. The trench axis is divided into the southern (black dots), central (orange), and northern N1 (purple) and N2 (red) segments. Also shown are the continent–ocean boundaries (COB, black dashed curves) and fossil ridges (black double lines). A total of 400 across-trench profiles were taken westward of the trench axis with the eastern ends of the profiles located at the Manila trench axis (marked by colour dots and shaded area). Each profile is perpendicular to the local strike of the trench axis. Every 10 individual profiles were grouped into a section with its eastern end marked by the connecting line between adjacent dots (e.g. Section 10, etc.). There are a total of 40 sections along the Manila Trench. (b) Sediment thickness of the study region with data from Yang *et al.* (2015). The northern Manila Trench north of 17.5°N is associated with an accretionary wedge. (c) The non-Airy-isostatic topographyof the study region, which was calculated by removing the isostatically compensated sediment thickness, crustal thickness and thermal subsidence from the observed topography. The non-Airy-isostatic topography was used as a reference to extract the *interpreted deformation* as a proxy for the overall shape of dynamically supported flexural bending topography. (d) The free-air gravity anomaly (FAA) of the study region, with data extracted from the global database of Sandwell *et al.* (2014).

**Table 3.** Best-fitting bending parameters of a global array of trenches.

| Section number | Trench name | Age (Ma) | $W_0$ (km) | $W_b$ (km) | $X_0$ (km) | $X_r$ (km) | $-V_0$ ($10^{12}$ N m$^{-1}$) | $M_0$ ($10^{16}$ N) | $T_e^M$ (km) | $T_e^m$ (km) | $T_e$ reduction (per cent) |
|---|---|---|---|---|---|---|---|---|---|---|---|
| 1 | Philippine | 68 | −0.9 | 0.40 | 35 | 45 | −0.3 | 8 | 57 | 22.8 | 60 |
| 2 | Philippine | 95 | −2.6 | 0.43 | 51 | 45 | −0.4 | 21 | 54 | 24.3 | 55 |
| 3 | Philippine | 99 | −2.6 | 0.22 | 31 | 40 | −0.3 | 11 | 48 | 16.8 | 65 |
| 4 | Kuril | 112 | −3.3 | 0.50 | 57 | 80 | 0.5 | 14 | 56 | 25.2 | 55 |
| 5 | Kuril | 118 | −4.2 | 0.17 | 79 | 100 | 2.0 | 7 | 35 | 24.5 | 30 |
| 6 | Japan | 126 | −2.6 | 0.10 | 65 | 80 | 0.3 | 17 | 56 | 30.8 | 45 |
| 7 | Japan | 132 | −2.7 | 0.23 | 93 | 115 | 1.8 | 0.1 | 40 | 22.0 | 45 |
| 8 | Izu-Bonin | 135 | −4.3 | 0.25 | 80 | 95 | 1.5 | 20 | 57 | 31.3 | 45 |
| 9 | Aleutian | 137 | −3.2 | 0.15 | 53 | 90 | 0.6 | 8 | 45 | 20.2 | 55 |
| 10 | Aleutian | 65 | −1.8 | 0.20 | 39 | 65 | −0.6 | 14 | 39 | 25.3 | 35 |
| 11 | Aleutian | 56 | −1.5 | 0.30 | 44 | 80 | 0.1 | 4 | 60 | 18.0 | 70 |
| 12 | Aleutian | 62 | −1.5 | 0.37 | 30 | 45 | −0.7 | 12 | 39 | 21.5 | 45 |
| 13 | Aleutian | 54 | −2.0 | 0.18 | 58 | 70 | 0.6 | 3 | 26 | 18.2 | 30 |
| 14 | Tonga | 104 | −3.3 | 0.20 | 49 | 60 | 0.3 | 15 | 64 | 22.4 | 65 |
| 15 | Kermadec | 96 | −3.5 | 0.33 | 61 | 70 | 1.2 | 5 | 37 | 18.5 | 50 |
| 16 | M. America | 19 | −2.0 | 0.12 | 39 | 35 | 0.2 | 3 | 23 | 11.5 | 50 |
| 17 | Peru | 27 | −1.3 | 0.29 | 53 | 50 | 0.3 | 2 | 23 | 16.1 | 30 |
| 18 | Chile | 49 | −2.7 | 0.30 | 48 | 70 | −0.1 | 17 | 58 | 26.1 | 55 |
| 19 | Chile | 39 | −2.4 | 0.14 | 58 | 60 | 0.3 | 11 | 48 | 24.0 | 50 |
| 20 | Sumatra | 125 | −1.5 | 0.19 | 52 | 70 | −0.4 | 17 | 55 | 33.0 | 40 |
| 21 | Java | 72 | −1.1 | 0.23 | 61 | 90 | −0.1 | 11 | 59 | 35.4 | 40 |
| 22 | S. Manila | 24 | −1.4 | 0.06 | 30 | 30 | 0.2 | 0.4 | 16 | 5.9 | 62 |
| 23 | C. Manila | 25 | −1.3 | 0.05 | 41 | 34 | 0.3 | 0.2 | 15 | 6.5 | 56 |
| 24 | N1. Manila | 32 | −0.5 | 0.05 | 47 | 50 | 0.2 | 0.3 | 15 | 10.7 | 29 |
| 25 | N2. Manila | 36 | −0.6 | 0.05 | 39 | 46 | 0.2 | 0.3 | 15 | 9.1 | 39 |
| 26 | S. Mariana | 150 | −4.2 | 0.36 | 77 | 88 | 1.3 | 15 | 48 | 27.1 | 43 |
| 27 | C. Mariana | 149 | −2.3 | 0.29 | 71 | 94 | 0.4 | 13 | 49 | 30.6 | 38 |
| 28 | N. Mariana | 142 | −1.8 | 0.29 | 67 | 86 | −0.02 | 16 | 49 | 35.4 | 28 |

2005; Wang *et al.* 2006, 2011; Zhao *et al.* 2010; Lin & Zhu 2015); $\bar{H}_c$ is the average thickness of the model oceanic crust and $\rho_w$, $\rho_s$, $\rho_c$ and $\rho_m$ are the densities of sea water, sediment, crust and mantle, respectively (Table 1).

*Non-Airy-isostatic topography:* we then calculated the non-Airy-isostatic topography of the Manila Trench ($T_{noniso}$, Fig. 3c) by removing the above calculated Airy local isostatic topography (i.e. eq. 1) and lithospheric thermal subsidence from the observed bathymetry. The calculation followed the methods outlined in Zhang *et al.* (2014):
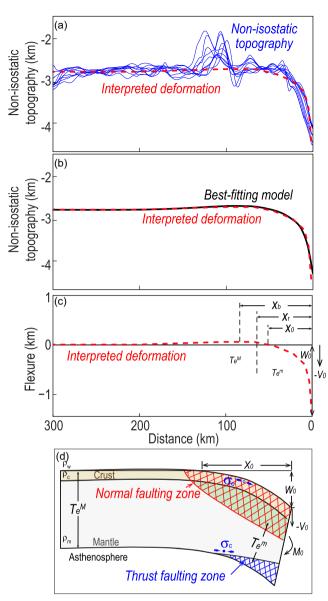
$$T_{noniso} = T_{topo} - T_{iso} - T_{sub}, \qquad (2)$$

where $T_{topo}$ is topography, and $T_{sub}$ is the lithospheric thermal subsidence calculated based on the crustal age map of the South China Sea (SCS) (Müller *et al.* 2008) and a half-space thermal cooling model of Turcotte & Schubert (2014). The calculated non-Airy-isostatic topography is a much-improved approximation for the flexural bending shape than the original bathymetry (Zhang *et al.* 2014). Along the Manila trench axis, the non-Airy-isostatic topography is deeper and narrower at the southern and central sections than that of the northern segments (Fig. 3c).

*Free-air gravity anomaly:* we also compared the non-Airy-isostatic topography with the free-air gravity anomaly (FAA), which Hunter & Watts (2016) used to model flexural bending. The FAA data (Fig. 3d) were extracted from the global database of Sandwell *et al.* (2014, http://topex.ucsd.edu/grav_outreach/index.html) with 1-min grid spacing. Our analysis revealed that the non-Airy-isostatic topography and free-air anomaly show similar overall spatial variations (Figs 3c and d and 5) although the FAA contains slightly less information due to upward attenuation of the gravity signal.

*Across-trench profiles:* we extracted 400 across-trench profiles along the Manila Trench. The location of the trench axis was defined as the deepest point along each profile. The spacing between two adjacent profiles is 2 km, and the length of each profile is 400 km. Every 10 profiles were grouped as a section, yielding a total of 40 sections (dots along the trench axis in Fig. 3). We found that many sections show the characteristic flexural bending shape (red curves in Fig. 5).

For each profile section of the Manila Trench, a best-fitting model for flexural bending was determined in two steps. (1) A smoothed *interpreted deformation* profile (red dashed curve in Figs 4a–c) was first constructed by fitting only the long-wavelength non-Airy-isostatic topography. Some large seamounts near the trench axis and their associated moats were difficult to be removed by mathematical filtering, and thus were visually bypassed using the 3-D topographic information of the trench valley. We used this *interpreted deformation* profile as an approximation for the flexural bending shape. (2) Grid search in parameter space (detailed in Section 2.3) was then conducted to find a best-fitting solution (black curve in Fig. 4b) that minimizes the root-mean-square (rms) misfit between the *interpreted deformation* shape and the theoretical models of flexural bending (red curves in Fig. 5). Through the above two-step analysis, we obtained a best-fitting model (red curves in Fig. 5) that can capture the long-wavelength characteristics of the non-Airy-isostatic topography (blue curves in Fig. 5) for each profile section.

The non-Airy-isostatic topography, interpreted plate deformation and best-fitting models were similarly obtained for the Mariana Trench by Zhang *et al.* (2014) and for the 11 additional trenches in this study (Fig. 6). The length of each across-trench profile is again 400 km.

**Figure 4.** (a) An example of non-Airy-isostatic topography profile and the *interpreted deformation*. Blue curves show an example of the calculated non-Airy-isostatic topography from Section 5 of Fig. 5. Red dashed line is the *interpreted deformation* that best represents the overall flexural bending shape. (b) The *interpreted deformation* profile (red dashed line) and the calculated best-fitting model (black line). The best-fitting model was calculated by inversion in flexural parameter space, yielding a theoretically predicted flexural bending profile that best matches the *interpreted deformation*. (c) Illustration of parameters: $X_b$ is the location of the shallowest point along the bending profile; $X_0$ is the location where vertical deformation $w = 0$; $X_r$ is the breaking point distance in the elastic plate thickness between the seaward ($T_e^M$) and trenchward ($T_e^m$) of the outer-rise region. (d) Schematic model of plate bending near a trench, showing expected extensional yield zone (red stripes) and compressional plastic deformation zone (blue stripes).

## 2.3 Flexural bending models

We consider a simplified model in which an elastic plate of variable effective elastic thickness $T_e(x)$ lies on top of inviscid asthenosphere (Fig. 4d). For each profile section, the variable $T_e(x)$ was further simplified into two characteristic constant $T_e$ values (Zhang *et al.* 2014). It is assumed that at a breaking point distance ($X_r$) near the outer-rise region (Fig. 4c), the elastic thickness seaward of the outer

rise ($T_e^M$) is reduced to that trenchward of the outer rise ($T_e^m$) due to pervasive faulting (Fig. 4d; Ludwig *et al.* 1966; Masson 1991; Ranero *et al.* 2003; Craig *et al.* 2014; Zhou *et al.* 2015; Hunter & Watts 2016). This approach with two $T_e$ values can simultaneously replicate the observed steep slope of the axial trench valley and the long-wavelength flexural bending seaward of the outer-rise region.

For each profile section, we inverted for five bending parameters that could best fit the *interpreted deformation* (Figs 4c and d): axial vertical loading ($-V_0$), axial bending moment ($M_0$), maximum effective elastic thickness ($T_e^M$), minimum effective elastic thickness($T_e^m$) and break point distance ($X_r$). The flexural bending parameters were inverted using the finite-difference numerical methods (Contreras-Reyes & Osses 2010; Zhang *et al.* 2014). The best-fitting model was obtained by searching for the solution that yielded the minimum rms between the interpreted deformation of the observed profiles and forward models. The detailed procedures of the analysis are described in Appendix B.

## 3 RESULTS

We compared the flexural bending of the Manila, Mariana and the global array of trenches to illustrates variability and common characteristics of the subduction systems. The trenches exhibit significant intratrench variations along both the Manila and Mariana Trenches (Figs 7 and 8) as well as significant intertrench variations among the global array of trenches (Fig. 8), thereby providing diverse examples for comparison.
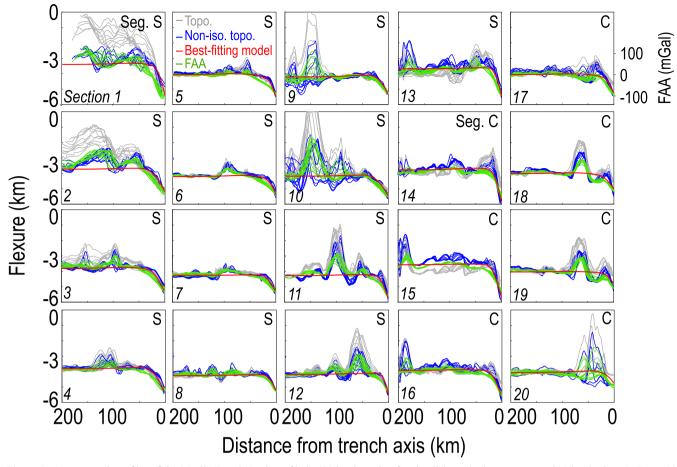
### 3.1 Best-fitting flexural bending solutions

*Manila Trench:* we obtained the best-fitting models (Fig. 5) and flexural bending parameters (Fig. 7) for individual profile sections of the Manila Trench (Tables 2 and C1). The trench relief ($W_0$) of the Manila is in the range of 0.4–2.1 km (Figs 7b and 8a and Table 2). The segment-averaged $W_0$ is larger for the S and C sections than the N1 and N2 segments. The Manila trench width ($X_0$) varies in the range of 20–66 km (Figs 7g and 8e), while the location of the shallowest bulge point ($X_b$) varies in the range of 60–111 km (Fig. 7h). The segment-averaged $X_0$ values for the S, C and N2 segments are smaller than those of the northern N1 segment.

The calculated axial vertical loading ($-V_0$) is in the range of 0–0.43 × $10^{12}$ Nm$^{-1}$ (Figs 7d and 8i) for the Manila Trench. The calculated axial bending moment ($M_0$) is in the range of 0–0.7 × $10^{16}$ N (Figs 7e and 8k). The calculated $T_e^M$ varies in the range of 14–24 km (Figs 7f and 8m) for profiles with relatively good constraints, while $T_e^m$ varies in the range of 4.8–13.5 km (Figs 7f and 8o). The above calculation yielded a reduction in $T_e$ of 25–70 per cent for the Manila Trench (Figs 7i and 8q). The transition from $T_e^M$ to $T_e^m$ occurs at $X_r$ of 15–80 km from the trench axis (Fig. 8g and Table C1).

*Mariana Trench:* the best-fitting bending parameters for the Mariana Trench (Table C2) were obtained by Zhang *et al.* (2014) using methods same as those described above. In general, the Manila Trench shows much greater values in trench depth, width and loading parameters (Figs 7 and 8).

*Global trenches:* analyses were conducted on a total of 21 global sections including the Philippine (Sections 1–3), Kuril (Sections 4 and 5), Japan (Sections 6 and 7), Izu-Bonin (Section 8), Aleutian (Sections 9–13), Tonga-Kermadec (Sections 14 and 15), Middle America (Section 16), Peru (Section 17), Chile (Sections 18 and 19), Sumatra (Section 20) and Java (Section 21) trenches. For the

**Figure 5.** Across-trench profiles of the Manila Trench (each profile is 400-km long, but for simplicity only the easternmost 200 km is shown). Every 10 individual profiles were stacked to form an averaged section. The Manila Trench consists of the southern segment (Sections 1–14), central segment (Sections 15–21), northern segment N1 (Sections 22–31) and northern segment N2 (Sections 32–40). In each section, light grey curves show the original bathymetry profiles. Blue curves are the calculated non-Airy-isostatic topography profiles. Green curves show the observed FAA profiles. Red curves show the *interpreted deformation* profiles that best capture the long-wavelength characteristics of the non-Airy-isostatic topography profiles. The *interpreted deformation* profiles were then used in the inversion of best-fitting flexural parameters for individual profile sections.

global array of trenches (Table 3), the section-averaged $W_0$ is in the range of 0.9–4.7 km (Fig. 8b), the average $X_0$ is in the range of 31–93 km (Fig. 8f). The average $T_e^M$ varies in the range of 23–60 km (Fig. 8n), while the average $T_e^m$ varies in the range of 11.5–35.4 km (Fig. 8p). The above calculations revealed a reduction in $T_e$ of 20–70 per cent with an average value of 47 per cent (Fig. 8r), which is consistent with the results of the circum-Pacific trenches (Hunter & Watts. 2016). The transition from $T_e^M$ to $T_e^m$ was calculated to be at $X_r$ of 35–115 km from the trench axis (Fig. 8h).

### 3.2 Comparisons between end-member examples

The end-member examples from the Manila and Mariana systems provide contrasting examples of flexural bending.

*Trench relief and width:* the range of $W_0$ of the Manila Trench (0.4–2.1 km) is similar to that of the Mariana N segment (0.9–2.1 km), but systematically smaller than that of the Mariana S (1.7–5.7 km) and C (1.5–3.8 km) segments (Fig. 7b and Table 2).

The range of the $X_0$ of the Manila Trench (20–66 km) is also smaller than that of most sections of the Mariana Trench (42–105 km, Table 2). The segment-averaged $X_0$ is similar among the southern (77 km), central (70 km) and northern (78 km) Mariana

segments. In comparison, the segment-averaged $X_0$ varies from the southern (33 km), central (41 km) and the northern Manila segments N1 (47 km) and N2 (36 km).

*Axial vertical loading and bending moment:* the trench-averaged axial vertical loading ($-V_0$) of the Manila Trench ($0.18 \times 10^{12}$ N m$^{-1}$) is 32 per cent, the average value of the Mariana Trench ($0.56 \times 10^{12}$ N m$^{-1}$, Fig. 7d). Lallemand *et al.* (2005) calculated the trench slab pulling force as $F = KL_d\sqrt{A}$, where $K$ is a constant, $L_d$ is the downdip slab length and $A$ is slab age. The slab pulling force of the Manila Trench ($7$–$16 \times 10^{12}$ N m$^{-1}$) was calculated to be 45 per cent that of the Mariana Trench ($19$–$31 \times 10^{12}$ N m$^{-1}$) (Lallemand *et al.* 2005), which is consistent with, although slightly greater than our calculated ratio of $-V_0$ of the two systems.

The trench-averaged axial bending moment of the Manila Trench ($0.31 \times 10^{16}$ N) is approximately 2.2 per cent that of the Mariana Trench ($1.41 \times 10^{17}$ N, Fig. 7e). The trench-averaged axial loading of the global array of trenches varies from $-0.7$ to $2.8 \times 10^{12}$ N m$^{-1}$ (Table 3).

The observed $W_0$ is, in general, positively correlated to the calculated $-V_0$ (Fig. 9a), while the observed height of the bulge ($W_b$) is positively correlated to $M_0$ (Fig. 9b). The best-fitting slopes of these parameters are larger for the Manila (black lines, Fig. 9) than the
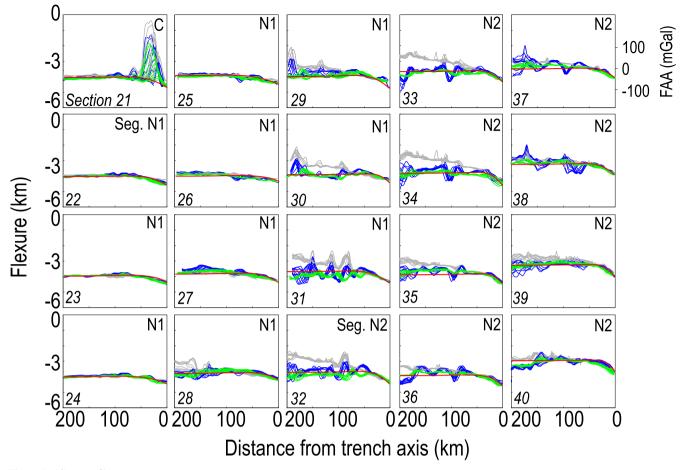
**Figure 5.** (*Continued.*)

Mariana Trench (red lines, Fig. 9), which is consistent with scaling laws, which predict steeper slopes for smaller average $T_e$ values (Turcotte & Schubert 2014).

### 3.3 Intertrench variations

*Global variability:* trench geometry and axial loadings exhibit a full spectrum of variation in bending parameters for the global array of trenches, facilitating further investigation. The $W_0$ of the global array of trenches is in the range of 0.9–4.7 km (Table 3). The trench width of the global array of trenches is in the range of 31–93 km (Table 3). Variations in $W_0$, $-V_0$ and $M_0$ of the Mariana Trench are almost as large as those of the global trenches (Fig. 8). However, variations in $X_0$, $X_r$, $T_e^m$ and $T_e^M$ of the Mariana Trench are smaller than the global trenches. Variations in all bending parameters of the Manila Trench are much smaller than the global trenches (Fig. 8).

*End-member groups:* the global trenches can be divided into three different groups. In the first end-member group of relatively young subducting plates, including the Middle America ($\sim$20 Ma) and Peru ($\sim$29 Ma) are associated with relatively small trench relief, width, effective elastic thickness and tectonic loadings. They are more similar to the Manila Trench (Fig. C1 and Table 3). In the second end-member group of relatively old subducting plates, trenches like Japan ($\sim$135 Ma) and Izu-Bonin($\sim$137 Ma) are associated with trench relief and width, effective elastic thickness and tectonic loadings. They are more similar to the Mariana Trench (Fig. C1 and Table 3). In the third group, values of plate age and

bending parameters are in between the end-member examples of the Manila and Mariana types (Fig. C1 and Table 3). These features indicate that in the cases of extremely young or old plates, the plate age could be a dominant factor in controlling the bending shape regardless the variations in axial loadings.

*Apparent shear and normal stresses:* we calculated the apparent axial shear stress $\sigma_s = -V_0/T_e^M$ and apparent axial normal stress $\sigma_n = 2M_0/(T_e^M)^2$. The axial shear stresses for the Manila, Mariana and global trenches have the range of 0 to 31, $-15$ to 66, $-15$ to 90 MPa, respectively (Figs 8s and t). The axial normal stresses for the Manila, Mariana and global trenches have the range of 0 to 71, 9 to 217 and 1 to 183 MPa, respectively (Figs 8u and v).

The apparent axial shear and normal stresses show much smaller variability (Figs 8s–v) than the $-V_0$ and $M_0$ (Figs 8i–l). These results indicate that while the average axial apparent shear stress is still slightly greater at the Mariana Trench than the Manila Trench, the much larger difference between the two trenches in $-V_0$ was largely due to the differences in plate thickness.

### 3.4 Synthesis 1: reduced elastic thickness $T_e^m$ controls near-trench bending

For a plate of constant elastic thickness, the trench relief ($W_0$) is calculated as follows (Turcotte & Schubert 2014):

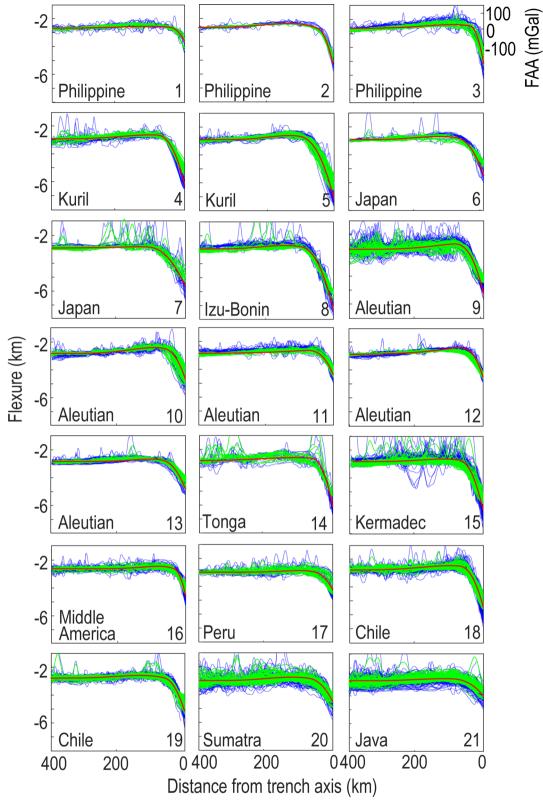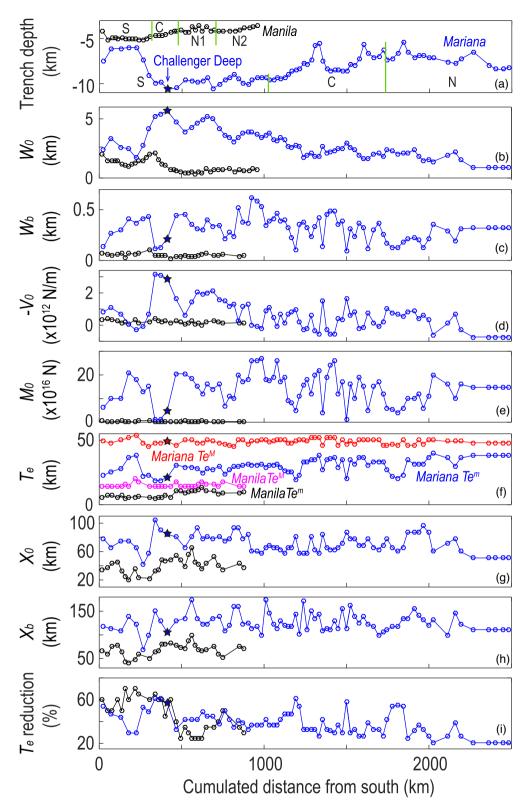$$W_0 = \frac{\alpha^2(V_0\alpha + M_0)}{2D}, \tag{3}$$

**Figure 6.** Across-trench profiles for each section of the global array of 11 trenches (each profile is 400-km long). Blue curves are the calculated non-Airy-isostatic topography profiles. Green curves show the observed FAA profiles. Red curves show the average *interpreted deformation* profiles that best capture the long-wavelength characteristics of the non-Airy-isostatic topography profiles. The *interpreted deformation* profiles were then used in the inversion of best-fitting flexural parameters for individual profile sections.

**Figure 7.** Calculated flexural bending parameters for individual across-trench profile sections along the Manila (black) and Mariana (blue) trenches. Star marks the profile section across the Challenger Deep area of the Mariana Trench. (a) Trench depth. The Manila Trench is divided into the southern (S), central (C) and northern (N1 and N2) segments, while the Mariana Trench consists of the southern (S), central (C) and northern (N) segments. (b) Trench relief ($W_0$), that is, trench axis depth relative to a far-field reference seafloor depth. (c) Bulge height ($W_b$), that is, depth of the shallowest point relative to a far-field reference seafloor depth. (d) Calculated axial vertical loading ($-V_0$). (e) Calculated axial bending moment ($M_0$). (f) Calculated elastic thickness seaward ($T_e^M$, purple) and trenchward ($T_e^m$, black) of the Manila Trench. Also shown are the values of elastic thickness seaward ($T_e^M$, red) and trenchward ($T_e^m$, blue) of the Mariana Trench. (g) Width of trench valley ($X_0$). (h) Location of the shallowest point along the bending profile ($X_b$). (i) Percentage reduction in the effective elastic thickness from $T_e^M$ to $T_e^m$. Note that data points with relatively poor constraints on key portions of the across-trench profile sections (marked in Table C1) were not plotted in panels (c)–(i) and Figs 8–11.
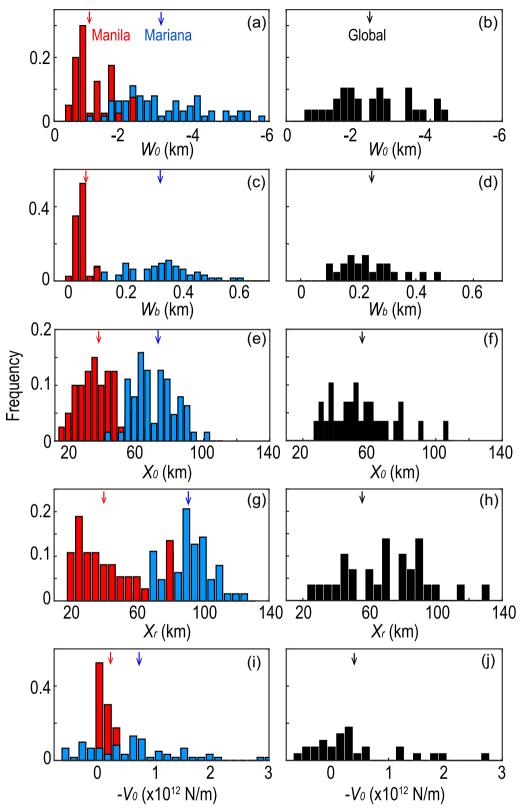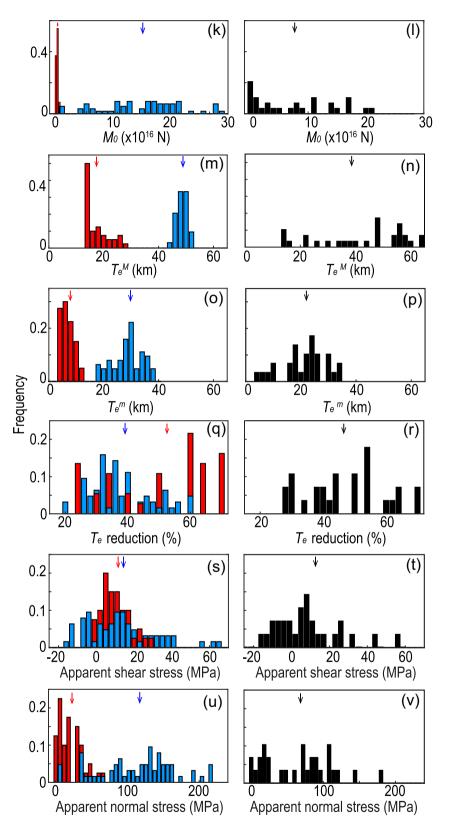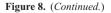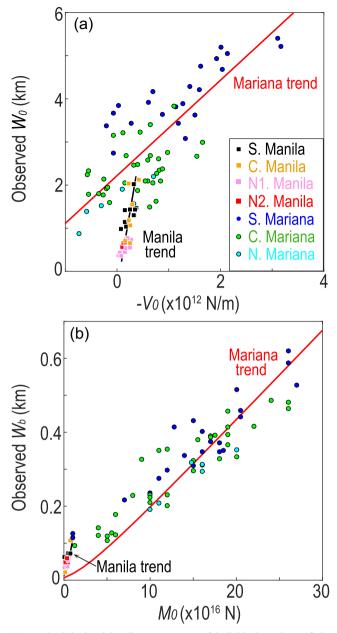
**Figure 8.** Statistics of trench geometry and bending parameters of the Manila (red), Mariana (blue) and global array of trenches (black). Arrows mark the average values.

**Figure 8.** (*Continued.*)

where flexural rigidity $D = \frac{E T_e^3}{12(1-v^2)}$ and the flexural wavelength $\alpha = [\frac{4D}{(\rho_m - \rho_w)g}]^{1/4}$ are a function of $T_e$; $E$ is Young's modulus, $v$ is Poisson's ratio, $g$ is gravity constant $\rho_m$ and $\rho_w$ are densities of mantle and sea water, respectively. We compared the observed $W_0$

with the predicted values for the end-member cases of $T_e = T_e^m$ and $T_e^M$, respectively, for the data sets of the Manila, Mariana and the global array of trenches. If the subducting plate is assumed to have a constant $T_e(x) = T_e^m$, the predicted $W_0$ values agree well with the observed values and are only slightly greater (by 9 per cent,

**Figure 9.** Calculated bending parameters of individual sections of the Manila and Mariana trenches. (a) Correlation between the axial vertical loading ($-V_0$) and observed trench relief ($W_0$). Also shown are the calculated relationships between $-V_0$ and $W_0$ for trench-averaged parameters for the Manila (black line) and Mariana (red line) trenches. (b) Correlation between the calculated axial bending moment ($M_0$) and observed bulge height ($W_b$). Also shown are the calculated relationships between $M_0$ and $W_b$ for trench-averaged parameters for the Manila (black line) and Mariana (red line) trenches.

Schubert [2014]):

$$X_0 = \alpha \tan^{-1}\left(1 + \frac{\alpha V_0}{M_0}\right) \qquad (4)$$

The predicted $X_0$ values assuming $T_e = T_e^m$ are on average only slightly greater (by 7 per cent) than the observed values of the Manila, Mariana and the global array of trenches (Fig. 10c). In contrast, the predicted $X_0$ values assuming $T_e = T_e^M$ would be on average much smaller (by 50 per cent) than the observed values (Fig. 10d). This implies that the observed $X_0$ is also controlled primarily by $T_e^m$ and affected only slightly by $T_e^M$.

For the case of $T_e = T_e^m$, the predicted cross-sectional areas of the trench valley, $S_0 = W_0 X_0 / 2$, are almost the same as the observed $S_0$ (Fig. 10e). Meanwhile, the predicted $S_0$ values assuming $T_e = T_e^M$ are on average only slightly smaller (by 14 per cent) than the observed $S_0$ (Fig. 10f). This implies that $S_0$ is only moderately sensitive to the choice of the $T_e$ values.

### 3.5 Synthesis 2: deepening and narrowing of trench valley caused by $T_e$ reduction

The reduction from $T_e^M$ to $T_e^m$ could cause significant deepening and narrowing of the trench valley (Fig. 11). We define the *absolute* value of the trench valley deepening as [$W_0$ increase] = [Observed $W_0$ − Calculated $W_0$ ($T_e^M$)], where $W_0$ ($T_e^M$) is the calculated $W_0$ when $T_e = T_e^M$ (Figs 11a–c). We also define the *relative* value of the trench valley deepening as [$W_0$ increase (per cent)] = [Observed $W_0$ − Calculated $W_0$ ($T_e^M$)]/[Calculated $W_0$ ($T_e^M$)] (Figs 11d–f).

For the Manila Trench, the predicted trench valley deepening is up to 1.4 km (Fig. 11a) or up to 177 per cent with an average value of 76 per cent (Fig. 11d). For the Mariana Trench, the predicted trench valley deepening is up to 2.8 km (Fig. 11b) or up to 183 per cent with an average value of 76 per cent (Fig. 11e). For the global array of trenches, the predicted trench valley deepening is up to 2.3 km (Fig. 11c) or up to 180 per cent with an average value of 88 per cent (Fig. 11f).
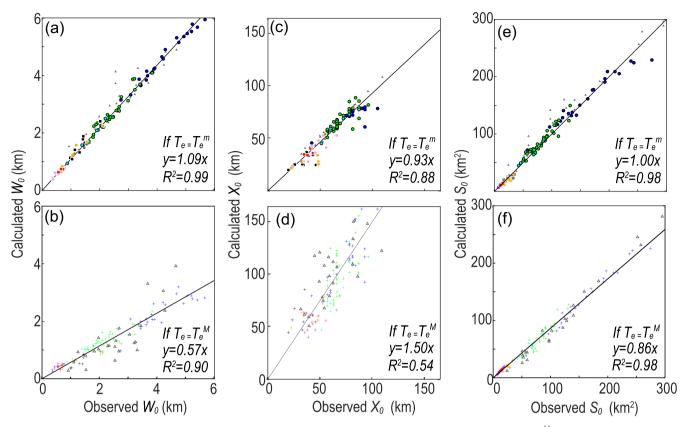
Similarly, the predicted trench valley narrowing for the Manila Trench is up to 49 km (Fig. 11g) or up to 62 per cent with an average value of 30 per cent (Fig. 11j). The predicted trench valley narrowing for the Mariana Trench is up to 72 km (Fig. 11h) or up to 53 per cent with an average value of 39 per cent (Fig. 11k). The predicted trench valley narrowing for the global array of trenches is up to 71 km (Fig. 11i) or up to 62 per cent with an average value of 37 per cent (Fig. 11l).

The above analyses thus provide important quantitative constraints on the strong links between plate bending, faulting-induced reduction in $T_e$, and changes in trench valley geometry. Flexural bending produces extensional stresses in the upper plate, which is responsible for the formation of normal faults (Fig. 4d). The bending-induced faults in turn reduce $T_e$, which further affects the trench geometry and dynamics in a positive feedback cycle (Fig. 4d). These relationships will be further discussed in Section 4.2.

## 4 DISCUSSION

### 4.1 Uncertainties in data analysis

The analyses of the Manila, Mariana and global array of trenches are associated with a number of uncertainties. For example, the calculated non-Airy-isostatic topography of the Manila Trench is associated with uncertainties in topography, sediment thickness,

Fig. 10a). In contrast, if the subducting plate is assumed to have a constant $T_e(x) = T_e^M$, the predicted $W_0$ values would much smaller (by an average of 43 per cent) than the observed values (Fig. 10b). This implies that the observed $W_0$ is indeed controlled primarily (more than 90 per cent) by $T_e^m$ and affected only slightly (less than 10 per cent) by $T_e^M$.

For a plate of constant elastic thickness, the width of the trench valley ($X_0$) is given by the following equation (Turcotte &

**Figure 10.** Illustration of the relative importance of $T_e^m$ (elastic thickness of the subducting plate reduced by faulting) versus $T_e^M$ (elastic thickness of unfaulted incoming plate) in controlling the trench relief (panels a and b), trench width (panels c and d) and area of the trench valley (panels e and f). Symbol colours of data points are the same as in Fig. 9. (a) and (b) Correlation between the observed trench relief ($W_0$) and the predicted $W_0$ for idealized cases assuming two constant elastic thickness: $T_e = T_e^m$ (solid dots, panel a) and $T_e = T_e^M$ (crosses, panel b). (c) and (d) Correlation between the observed trench width ($X_0$) and the predicted $X_0$ for the cases of $T_e = T_e^m$ (solid dots, panel c) and $T_e = T_e^M$ (crosses, panel d). (e) and (f) Correlation between the observed cross-sectional area of the trench valley, defined as $S_0 = W_0 X_0/2$, and the predicted $S_0$ for the cases of $T_e = T_e^m$ (solid dots, panel e) and $T_e = T_e^M$ (crosses, panel f). Note that the observed $W_0$ (panel a) and $X_0$ (panel c) can both be explained primarily by models assuming the (i.e. $T_e = T_e^m$). The observed $S_0$ (panel e) can also be fitted slightly better by models assuming $T_e = T_e^m$.

gravity-derived crustal thickness, manual choice of the *interpreted deformation* profiles and 3-D effects of plate bending (Manríquez *et al.* 2014). We have examined several alternative models of Manila sediment and crustal thickness, and found that the overall Manila parameters stay unchanged, indicating that our results are relatively robust. Furthermore, the overall spatial variations of the calculated non-Airy-isostatic topography match well with that of the FAA (Fig. 5). Similarly, the uncertainties in the calculation of non-Airy-isostatic topography of the Mariana Trench were discussed in detail in Zhang *et al.* (2014), while the uncertainties associated with the global array of trenches were difficult to quantify at this point.
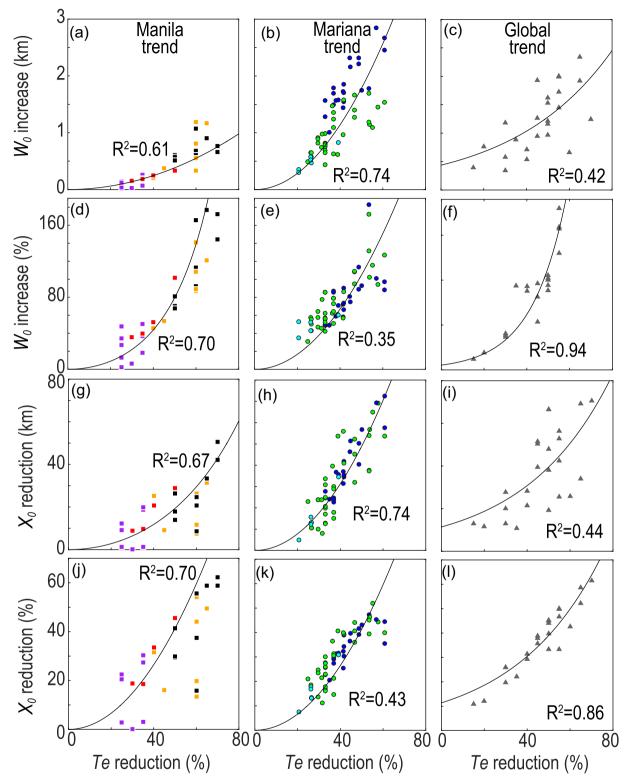
Normal faults of both the Manila and Mariana Trenches were found to distribute over a broad region from the outer-rise region to the trench axis. In areas with good multibeam bathymetry coverage (Barckhausen *et al.* 2014; Zhang *et al.* 2014), our analysis revealed that the location of the calculated $X_r$ is in general consistent with the observed outer boundary of the surficial normal faulting zones, providing further confidence in the overall results.

### 4.2 Flexural bending of elastic versus elastoplastic plates

To better understand the implications of the modeling results of this study, we investigated the role of plastic yielding in the reduction of $T_e$. We first obtained the smoothed flexural bending

shape ($w$) of an example profile with relatively good data quality from the S. Mariana Trench (section 10 in Zhang *et al.* 2014, black curve, Fig. 12a). We then calculated the curvature of this profile by $\kappa = d^2w/dx^2$ (Fig. 12b). The expected stress distribution with depth in an elastoplastic plate is shown in Fig. 12(c). Take the depth profile at across-trench distance of 100 km as an example (blue profile 2, Fig. 12c): it is anticipated that the upper plate would be under extension, while the lower plate under compression (Fig. 12c).

When the deviatoric stresses exceed the yield stress envelope, brittle failure could occur in the elastic upper plate by frictional faulting and earthquakes, while plastic deformation could occur in the lower layer according to temperature-dependent power-law rheology (Goetze 1978; Goetze & Evans 1979; Kirby 1983; Chen & Morgan 1990). The maximum sustainable deviatoric stresses in the brittle yield zone of the upper plate is controlled by maximum shear stress $\Delta\tau = \mu(\sigma_n - P_f)$, where $\mu$ is rock frictional coefficient, $\sigma_n$ is normal stress and $P_f$ is pore fluid pressure on the fault plane. Meanwhile, an elastic core at the central depth is expected to be sandwiched between the upper brittle yield zone and the lower layer of plastic deformation (Figs 12c and d). The slope of the elastic core $\kappa$ shown in Fig. 12(c) is constrained by the observed flexural shape of the S. Mariana Trench (Fig. 12a). The calculated deviatoric stress as a function of distance from the trench axis is shown in Fig. 12(d).

**Figure 11.** Predicted deepening in the trench valley ($W_0$ increase, panels a–f) and narrowing in the trench valley ($X_0$ decrease, panels g–l) due to $T_e$ reduction. Symbols of data points are the same as in Fig. 9. (a)–(c) The predicted *absolute* value of trench valley deepening is defined as [$W_0$ increase (km)] = [Observed $W_0$]—[Calculated $W_0$ ($T_e^M$)], where $W_0$ ($T_e^M$) is the calculated $W_0$ without faulting-induced $T_e$ reduction. (d)–(f) The predicted *relative* value of the trench valley deepening is defined as [$W_0$ increase (per cent)] = [Observed $W_0$ – Calculated $W_0$ ($T_e^M$)]/[Calculated $W_0$ ($T_e^M$)]. (g)–(i) The predicted *absolute* value of the trench valley narrowing is defined as [$X_0$ reduction (km)] = [Observed $X_0$ –Calculated $X_0$ ($T_e^M$)]. (j)–(l) The predicted *relative* value of the trench valley narrowing is defined as [$X_0$ reduction (per cent)] = [Observed $X_0$ – Calculated $X_0$ ($T_e^M$)]/[Calculated $X_0$ ($T_e^M$)]. Also shown are the best-fitting curves using the formula $y = A1*\exp(A2\,x^2 - 1)$, where $A1$ and $A2$ are the best-fitting coefficients.
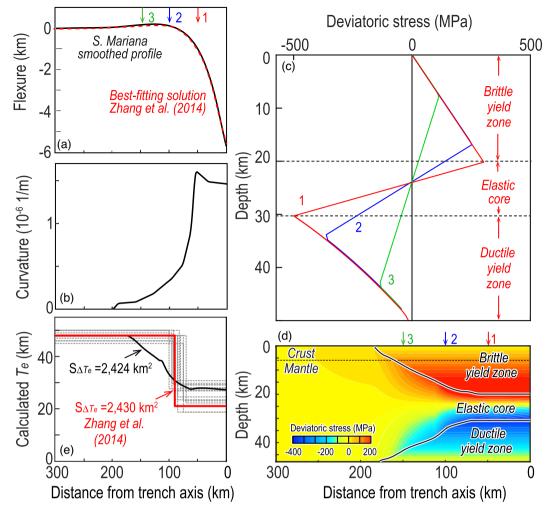
**Figure 12.** (a) Smoothed flexural bending shape ($w$) of an example profile from the southern Mariana Trench (section 10 in Zhang *et al*. 2014). (b) Calculated curvatures of the example profiles of the Mariana Trench, which was calculated by $k = d^2w/dx^2$. (c) Calculated deviatoric stresses as a function of depth in the subducting plate at distance of 50, 100 and 150 km from the trench axis. The lithosphere consists of the upper yield zone, central elastic core and lower ductile layer. (d) Cross-section of the calculated deviatoric stresses for the example profile shown in panel (a). (e) Calculated models of $T_e$ as a function of the distance from the trench axis for the example profile. Note that the solutions for thin plate bending of an elastoplastic plate (thick black curve) and the thin plate bending assuming two $T_e$ values (red curve) yield similar $T_e$ reduction surface $S_{\Delta Te}$, illustrating that $S_{\Delta Te}$ is a relatively good measure of the overall effect of plate weakening on flexural bending shape. Thin dashed black lines show results of other profiles of the southern Mariana Trench from Zhang *et al*. (2014).

Our numerical models calculated the deviatoric stress of the subducting plate (Fig. 12d), from which we obtained the bending moment $M(x)$ by integrating the deviatoric stress and the vertical depth distance from the neutral plane as follows:

$$M = \int_0^{T_e} \Delta\sigma_{xx}(y - y_n)dy, \tag{5}$$

where $\Delta\sigma_{xx}$ is the horizontal deviatoric stress in the plate, $E$ is Young's modulus, $y$ is the depth and $y_n$ is the depth of the neutral plane. Furthermore, we calculated the plate curvature $\kappa$ from the slope of the deviatoric stress in the elastic core (e.g. Hunter & Watts 2016) as follows:

$$\Delta\sigma_{xx}^{elastic} = \frac{E(y - y_n)\kappa}{1 - v^2}, \tag{6}$$

We then obtained the flexural rigidity $D$ according to the following (Turcotte & Schubert 2014):

$$M = -D\frac{d^2w}{dx^2} = D\kappa, \tag{7}$$

Finally, the effective elastic plate thickness $T_e$ was calculated via $T_e = \left[\frac{12(1-v^2)D}{E}\right]^{\frac{1}{3}}$ (thick black curve, Fig. 12e).

Here, we introduce a new parameter called *$T_e$ reduction area* $S_{\Delta Te} = \int_0^{Xr}[T_e^M - T_e(x)]dx = (T_e^M - T_e^m)X_r$, which is the integrated amount of $T_e$ reduction along the across-trench profile. Thus, the calculated $T_e^m$ represents the *average* reduced $T_e$ trenchward of the outer-rise region.

The above analysis illustrated that the calculated reduction in $T_e$ for this example profile (Section 10) in the S. Mariana Trench is about 43.8 per cent over a distance of 60–170 km (thick black curve, Fig. 12e), and the calculated $S_{\Delta Te}$ is 2424 km². Meanwhile, the inverted $T_e^M$ to $T_e^m$ reduction for the same Section 10 of the S. Mariana Trench was about 56.9 per cent with a break point distance of 90 km (thick red curve, Fig. 12e), and the calculated $S_{\Delta Te}$ is 2430 km². The similarity in $S_{\Delta Te}$ from the two different methods illustrate that our simplification of using two $T_e$ values can produce results that are comparable, at least qualitatively, to the results from the elastoplastic deformation of a plate. The calculated stresses and

geometry of the yield zones (Fig. 12d) also provide a mechanical basis for the conceptual model shown in Fig. 4(d).

## 5 CONCLUSIONS

Detailed analyses of a global array of trenches revealed systematic *intra-* and *intertrench* variations with implications on trench dynamics:

(1) The relatively young subducting plates (e.g. the Manila, Middle America and Peru Trenches) show systematically small elastic thickness ($T_e^M$ and $T_e^m$) and bending wavelengths ($X_0$, $X_r$ and $\alpha$). In contrast, the relatively old subducting plates (e.g. the Mariana, Japan and Izu-Bonin Trenches) show systematically large elastic thickness and bending wavelengths. These features indicate that in the cases of extremely young or old plates, the plate age could be a dominant factor in controlling the bending shape regardless the variations in axial loadings.

(2) In the end-member case of the Mariana Trench, the *intra-trench* variations in trench relief ($W_0$), bulge height ($W_b$), axial vertical loading ($-V_0$) and bending moment ($M_0$) are as large as the *intertrench* variations in the section-averaged values of the global array of trenches. The calculated apparent normal ($\sigma_n$) and shear ($\sigma_s$) stresses for the Mariana Trench also show variations as large as that of the global trenches, indicating that the axial loading and stresses of old subducting plates can vary significantly along the trench axis. In contrast, the young subducting plates show much smaller values and variations in the axial loading ($-V_0$ and $M_0$) and stresses ($\sigma_n$ and $\sigma_s$).

(3) For all trenches, $W_0$ and $X_0$ were found to be controlled primarily by $T_e^m$ (91 per cent and 93 per cent, respectively) and affected only slightly by $T_e^M$ (9 per cent and 7 per cent, respectively). Thus, the $T_e^m$ controls the near-axis trench geometry.

(4) The faulting-induced reduction from $T_e^M$ to $T_e^m$ was estimated to be 25 per cent–70 per cent (average 48 per cent) for the Manila Trench, 21 per cent–61 per cent (average 39 per cent) for the Mariana Trench and 20 per cent–70 per cent (average 47 per cent) for the global array of trenches, indicating the universal importance of faulting in $T_e$ reduction.

(5) Comparing to the case of unfaulted subducting plate, $T_e$ reduction increases the trench depth $W_0$ by an average of 76 per cent for both the Manila and Mariana trenches and 88 per cent for the global trenches. The calculated average decrease in trench width $X_0$ due to $T_e$ reduction is 30 per cent, 39 per cent and 37 per cent for the Manila, Mariana and global trenches, respectively.

## REFERENCES

Arredondo, K.M. & Billen, M.I., 2012. Rapid weakening of subducting plates from trench-parallel estimates of flexural rigidity, *Phys. Earth planet. Inter.,* **196**, 1–13.

Billen, M.I. & Gurnis, M., 2005. Constraints on subducting plate strength within the Kermadec trench, *J. geophys. Res.,* **110**(B5), 119–142.

Barckhausen, U., Engels, M., Franke, D., Ladage, S. & Pubellier, M., 2014. Evolution of the South China Sea: revised ages for breakup and seafloor spreading, *Mar. Petrol. Geol.,* **58**, 599–611.

Bird, P., 2003. An updated digital model of plate boundaries, *Geochem. Geophys. Geosyst.,* **4**(3), 1027, doi:10.1029/2001GC000252.

Bodine, J.H. & Watts, A.B., 1979. On lithospheric flexure seaward of the Bonin and Mariana trenches, *Earth planet. Sci. Lett.,* **43**(1), 132–148.

Boston, B., Moore, G.F., Nakamura, Y. & Kodaira, S., 2014. Outer-rise normal fault development and influence on near-trench décollement propagation along the Japan Trench, off Tohoku, *Earth Planet Space.,* **66**(1), 1–17.

Briais, A., Patriat, P., Tapponnier & P., 1993. Updated interpretation of magnetic anomalies and seafloor spreading stages in the South China Sea: implications for the Tertiary tectonics of Southeast Asia, *J. geophys. Res.,* **98**(B4), 6299–6328.

Bry, M. & White, N., 2007. Reappraising elastic thickness variation at oceanic trenches, *J. geophys. Res.,* **112**(B8), 582–596.

Caldwell, J.G., Haxby, W.F., Karig, D.E. & Turcotte, D.L., 1976. On the applicability of a universal elastic trench profile, *Earth planet. Sci. Lett.,* **31**(2), 239–246.

Chen, Y. & Morgan, W.J., 1990. A nonlinear rheology model for mid-ocean ridge axis topography, *J. geophys. Res.,* **95**(B11), 17 583–17 604.

Contreras-Reyes, E. & Osses, A., 2010. Lithospheric flexure modelling seaward of the Chile trench: implications for oceanic plate weakening in the trench outer rise region, *Geophys. J. Int.,* **182**, 97–112.

Contreras-Reyes, E., Jara, J., Maksymowicz, A. & Weinrebe, W., 2013. Sediment loading at the southern Chilean trench and its tectonic implications, *J. Geodyn.,* **66**, 134–145.

Craig, T.J., Copley, A. & Jackson, J., 2014. A reassessment of outer-rise seismicity and its implications for the mechanics of oceanic lithosphere, *Geophys. J. Int.,* **197**(1), 63–89.

Divins, D., 2003. *Total Sediment Thickness of the World's Oceans and Marginal Seas,* NOAA National Geophysical Data Center.

Eakin, D.H., McIntosh, K.D., Van Avendonk, H., Lavier, L., Lester, R., Liu, C.S. & Lee, C.S., 2014. Crustal-scale seismic profiles across the Manila subduction zone: the transition from intraoceanic subduction to incipient collision, *J. geophys. Res.,* **119**(1), 1–17.

Gou, F., Kodaira, S., Yamashita, M., Sato, T., Takahashi, T. & Takahashi, N., 2013. Systematic changes in the incoming plate structure at the Kuril trench, *Geophys. Res. Lett.,* **40**(1), 88–93.

Galgana, G., Hamburger, M., McCaffrey, R., Corpuz, E. & Chen, Q., 2007. Analysis of crustal deformation in Luzon, Philippines using geodetic observations and earthquake focal mechanisms, *Tectonophysics.,* **432**(1–4), 63–87.

Goetze, C., 1978. The mechanisms of creep in olivine [and discussion], *Phil. Trans. R. Soc. Lond.,* **288**(1350), 99–119.

Goetze, C. & Evans, B., 1979. Stress and temperature in the bending lithosphere as constrained by experimental rock mechanics, *Geophys. J. R. astr. Soc.,* **59**(3), 463–478.

Hanks, T.C., 1971. The Kuril Trench - Hokkaido rise system: large shallow earthquakes and simple models of deformation, *Geophys. J. R. astr. Soc.,* **23**(2), 173–189.

Harris, R. & Chapman, D., 1994. A comparison of mechanical thickness estimates from trough and seamount loading in the southeastern Gulf of Alaska, *J. geophys. Res.,* **95**(B5), 9297–9317.

Hayes, D.E. & Lewis, S.D., 1984. A geophysical study of the Manila Trench, Luzon, Philippines: 1. Crustal structure, gravity, and regional tectonic evolution, *J. geophys. Res.,* **89**(B11), 9171–9195.

Hayes, D.E. & Nissen, S.S., 2005. The South China Sea margins: implications for rifting contrasts, *Earth planet. Sci. Lett.,* **237**(3–4), 601–616.

Hunter, J. & Watts, A.B., 2016. Gravity anomalies, flexure and mantle rheology seaward of circum-Pacific trenches, *Geophys. J. Int.,* **207**(1), 288–316.

Jones, G.M., Hilde, T.W.C., Sharman, G.F. & Agnew, D.C., 1978. Fault patterns in outer trench walls and their tectonic significance, *J. Phys. Earth,* **26**(Suppl.), S85–S101.

Kirby, S.H., 1983. Rheology of the lithosphere, *Rev. Geophys.,* **21**(6), 1458–1487.

Kuo, B.-Y. & Forsyth, D.W., 1988. Gravity anomalies of the ridge-transform system in the South Atlantic between 31° and 34.5°S: upwelling centers and variations in crustal thickness, *Mar. Geophys. Res.,* **10**, 205–232.

Lallemand, S., Heuret, A. & Boutelier, D., 2005. On the relationships between slab dip, back-arc stress, upper plate absolute motion, and crustal nature in subduction zones, *Geochem. Geophys. Geosyst.,* **6**, Q09006, doi:1029/2005GC000917.

Li, C. *et al.*, 2014. Ages and magnetic structures of the South China Sea constrained by deep tow magnetic surveys and IODP Expedition 349, *Geochem. Geophys. Geosyst.,* **15**, 4958–4983.

Li, C. *et al.*, 2015. Seismic stratigraphy of the central South China Sea basin and implications for neotectonics, *J. geophys. Res.,* **120**, 1377–1399.

Lin, J.Y., 2015. Megathrust earthquake potential of the Manila subduction system: revealed by the seismic moment tensor element Mrr, *Terr. Atoms. Ocean. Sci.,* **26**, 619–630.

Lin, J. & Zhu, J., 2015. Global variations in gravity-derived oceanic crustal thickness and implications on oceanic crustal accretion processes (abstract), in *AGU Fall Meeting,* V14A-07.

Ludwig, W.J. *et al.*, 1966. Sediments and structure of the Japan trench, *J. geophys. Res.,* **71**, 2121–2137.

Manríquez, P., Contreras-Reyes, E. & Osses, A., 2014. Lithospheric 3-D flexure modelling of the oceanic plate seaward of the trench using variable elastic thickness, *Geophys. J. Int.,* **196**, 681–693.

Masson, D.G., 1991. Fault patterns at outer trench walls, *Mar. Geophys. Res.,* **13**, 209–225.

McAdoo, D.C., Caldwell, J.G. & Turcotte, D.L., 1978. On the elastic-perfectly plastic bending of the lithosphere under generalized loading with application to the Kuril Trench, *Geophys. J. Int.,* **54**, 11–26.

Molnar, P. & Atwater, T., 1978. Interarc spreading and Cordilleran tectonics as alternates related to the age of subducted oceanic lithosphere, *Earth planet. Sci. Lett.,* **41**, 330–340.

Müller, R.D., Sdrolias, M., Gaina, C. & Roest, W.R., 2008. Age, spreading rates, and spreading asymmetry of the world's ocean crust, *Geochem. Geophys. Geosyst.,* **9**, doi:10.1029/2007GC001743.

Naliboff, J.B., Billen, M.I., Gerya, T. & Saunders, J., 2013. Dynamics of outer-rise faulting in oceanic-continental subduction systems, *Geochem. Geophys. Geosyst.,* **14**, 2310–2327.

Obana, K. *et al.*, 2012. Normal-faulting earthquakes beneath the outer slope of the Japan Trench after the 2011 Tohoku earthquake: implications for the stress regime in the incoming Pacific plate, *Geophys. Res. Lett.,* **39**, L00G24, doi:10.1029/2011GL050399.

Parker, R.L., 1973. The rapid calculation of potential anomalies, *Geophys. J. R. astr. Soc.,* **31**, 447–455.

Qiu, X.L., Ye, S., Wu, S., Shi, X. & Zhou, D., 2001. Crustal structure across the Xisha trough, northwestern South China Sea, *Tectonophysics,* **341**, 179–193.

Ranero, C.R., Morgan, J.P., Mclntosh, K. & Reichert, C., 2003. Bending-related faulting and mantle serpentinization at the Middle America trench, *Nature,* **425**, 367–373.

Ranero, C.R., Villaseor, A., Morgan, J.P. & Wdinrebe, W., 2005. Relationship between bend-faulting at trenches and intermediate-depth seismicity, *Geochem. Geophys. Geosyst.,* **6**, doi:10.1029/2005GC000997.

Rangin, C., Le Pichon, X., Mazzotti, S., Pubellier, M., Chamot-Rooke, N., Aurelio, M., Walpersdorf, A. & Quebral, R., 1999. Plate convergence measured by GPS across the Sundaland/Philippine Sea Plate deformed boundary: the Philippines and eastern Indonesia, *Geophys. J. Int.,* **139**, 296–316.

Sandwell, D.T., Müller, R.D., Smith, W.H., Garcia, E. & Francis, R., 2014. New global marine gravity model from CryoSat-2 and Jason-1 reveals buried tectonic structure, *Science,* **346**, 65–67.

Sibuet, J.C., Yeh, Y.C. & Lee, C.S., 2016. Geodynamics of the South China Sea, *Tectonophysics,* **692**, 98–119.

Smith, W.H. & Sandwell, D.T., 1997. Global sea floor topography from satellite altimetry and ship depth soundings, *Science,* **277**, 1956–1962.

Turcotte, D., McAdoo, D. & Caldwell, J., 1978. An elastic-perfectly plastic analysis of the bending of the lithosphere at a trench, *Tectonophysics,* **47**, 193–205.

Turcotte, D. & Schubert, G., 2014. *Geodynamics,* 3rd edn, Cambridge Univ. Press, 456 pp.

Walcott, R.I., 1970. Flexural rigidity, thickness, and viscosity of the lithosphere, *J. geophys. Res.,* **75**, 3941–3954.

Wang, T.K., Chen, M.K., Lee, C.S & Xia, K., 2006. Seismic imaging of the transitional crust across the northeastern margin of the South China Sea, *Tectonophysics,* **412**, 237–254.

Wang, T., Lin, J., Tucholke, B. & Chen, Y.J., 2011. Crustal thickness anomalies in the North Atlantic Ocean basin from gravity analysis, *Geochem. Geophys. Geosyst.,* **12**, doi:10.1029/2010GC003402.

Watts, A.B., 2001. *Isostasy and Flexure of the Lithosphere,* Cambridge Univ. Press, 458 pp.

Watts, A.B. & Talwani, M., 1974. Gravity anomalies seaward of deep-sea trenches and their tectonic implications, *Geophys. J. Int.,* **36**, 57–90.

Yan, P., Zhou, D. & Liu, Z., 2001. A crustal structure profile across the northern continental margin of the South China Sea, *Tectonophysics,* **338**, 1–21.

Yang, S., Qiu, Y. & Zhu, B., 2015. *Atlas of Geology and Geophysics of the South China Sea,* China Navigation Publications.

Yu, H., 2000. Closure of Manila Trench north of Latitude 21°N in transition of passive-convergent margin south of Taiwan, *Acta Oceanogr. Taiwan,* **38**, 115–127.

Zhang, F., Lin, J. & Zhan, W., 2014. Variations in oceanic plate bending along the Mariana trench, *Earth planet. Sci. Lett.,* **401**, 206–214.

Zhao, M.H., Qiu, X., Xia, S., Xu, H. & Wang, P., 2010. Seismic structure in the northeastern South China Sea: S-wave velocity and Vp/Vs ratios derived from three-component OBS data, *Tectonophysics,* **480**, 183–197.

Zhou, Z., Lin, J., Behn, M.D. & Olive, J.A., 2015. Mechanism for normal faulting in the subducting plate at the Mariana Trench, *Geophys. Res. Lett.,* **42**, 4309–4317.

# APPENDIX A: CALCULATION OF CRUSTAL THICKNESS

The gravity-derived crustal thickness was used in the calculation of non-Airy-isostatic topography in the main text. Here, we show the procedure of the calculation and assumptions. The crustal thickness model was calculated following the procedure of Kuo & Forsyth (1988).

(1) *Mantle Bouguer gravity anomaly*: we first calculated mantle Bouguer anomaly (MBA) by removing from the FAA the gravitational effects of sea water-sediment, sediment-crust and crust–mantle interfaces by assuming a reference model of crustal thickness.

(2) *Thermal correction*: we calculated 3-D mantle temperature field of a 100-km-thick mantle layer by assuming 1-D vertical cooling (Turcotte & Schubert 2014) and using the plate-age data of Müller *et al.* (2008). The top and bottom temperatures of the mantle layer were assumed to be $T_0 = 0\,°C$ and $T_m = 1350\,°C$, respectively. We then converted the thermal structure into a 3-D grid by $\Delta \rho = \rho - \rho_0 = -\alpha \rho_0 (T - T_0)$, where $T_0 = 1350\,°C$ and $\rho_0 = 3.3 \times 10^3$ kg m$^{-3}$ are the reference values of mantle temperature and density, respectively, while $\alpha = 3 \times 10^{-5}$ K$^{-1}$ is the thermal expansion coefficient.

(3) *Residual mantle Bouguer anomaly*: we then removed the calculated lithospheric cooling effects from the MBA to obtain the residual mantle Bouguer anomaly (RMBA).

**Figure A1.** Flexural deformation of the Manila (red), Mariana (blue), Middle America (green), Peru (orange), Japan (purple), Izu-Bonin (black) and other (grey) trenches.

(4) *Crustal thickness model*: finally, we calculated models of crustal thickness variations by downward continuation of the RMBA signals to a constant-reference depth (e.g. Parker 1973; Kuo & Forsyth 1988; Wang *et al.* 2011; Lin & Zhu 2015). The best-fitting parameters in the gravity modeling, including the mantle and crust densities used in the gravity model, were obtained from comparison with available seismic profiles in the SCS (Qiu *et al.* 2001; Yan *et al.* 2001; Hayes & Nissen 2005; Wang *et al.* 2006; Zhao *et al.* 2010).

## APPENDIX B: MODELING OF FLEXURAL BENDING

Flexural bending of a thin plate can be described by the following equation (Turcotte & Schubert 2014):

$$-\frac{d^2 M}{dx^2} + \frac{d}{dx}\left(F\frac{dw}{dx}\right) + \Delta\rho g w = q, \tag{B1}$$

where $M$ is bending moment, $F$ is horizontal force, $\Delta\rho g w = (\rho_{\mathrm{m}} - \rho_{\mathrm{w}})g w(x)$ is restoring force and $q(x)$ is vertical sediment loading. In this study, the effect of the sediment loading was already accounted for in the calculation of non-Airy-isostatic topography by assuming the sediment loading is Airy isostatically compensated. Thus, we used $q = 0$ during parameter inversion. The bending moment is related to the plate vertical deflection by

$$M = -D\frac{d^2 w}{dx^2}, \tag{B2}$$

where flexural rigidity is $D = \frac{E T_e^3}{12(1-v^2)}$, $E$ represents Young's modulus, $v$ is Poisson's ratio and $T_e$ is effective elastic thickness. The vertical loading $V$ is related to bending moment and horizontal force:

$$V = \frac{dM}{dx} - F\frac{dw}{dx}, \tag{B3}$$

The horizontal force $F$ is assumed to be small in accordance with previous studies (Caldwell *et al.* 1976; Molnar & Atwater 1978; Contreras-Reyes & Osses 2010). The constant parameters assumed in this study are listed in Table 1. The boundary conditions are as follows:

$$w = 0|_{x=+\infty}, \tag{B4}$$

$$\frac{dw}{dx} = 0|_{x=+\infty}, \tag{B5}$$

$$-M_0 = D\frac{d^2 w}{dx^2}|_{x=0}, \tag{B6}$$

$$-V_0 = \frac{dM}{dx}|_{x=0}, \tag{B7}$$

Assuming that the spatial variation in the horizontal force, $dF(x)/dx$ is relatively small, eq. (B3) can be rewritten as a set of second-order differential equations (Contreras-Reyes & Osses 2010):

$$\frac{d^2 w}{dx^2} = -\frac{M}{D}, \tag{B8}$$

$$\frac{d^2 M}{dx^2} = -F\frac{M}{D} + \Delta\rho g w - q, \tag{B9}$$

where $\Delta\rho = \rho_{\mathrm{m}} - \rho_{\mathrm{w}}$ and $q = 0$ in this study.

We solved for the following variables: $-V_0$, $M_0$, $T_e^M$, $T_e^m$ and $X_r$, using a finite-difference method (Contreras-Reyes & Osses 2010) with technical details described in Zhang *et al.* (2014). Comparing to previous studies (Bodine & Watts 1979; Bry & White 2007; Turcotte & Schubert 2014), this approach has a number of advantages: (1) the effects of sediment loading and crustal thickness variations were modeled by assuming Airy isostatic compensation; and (2) the observed steep slope trenchward of the outer-rise, as well as the relatively long flexural wavelength seaward of the outer-rise region can be replicated simultaneously by using an elastic plate of two constant values of $T_e^M$ and $T_e^m$. The sensitivity of flexural bending to the assumed forms of spatial variations in $T_e^m$ is discussed in Figs 5(a) and (b) of the main text.

# APPENDIX C: BENDING PARAMETERS OF THE MANILA AND MARIANA TRENCHES

**Table C1.** Best-fitting bending parameters of the Manila Trench.

| Section quality | Cumulated distance (km) | $W_0$ (km) | $W_b$ (km) | $X_0$ (km) | $X_r$ (km) | $-V_0$ ($10^{12}$ N m$^{-1}$) | $M_0$ ($10^{16}$ N) | $T_e^M$ (km) | $T_e^m$ (km) | $T_e$ reduction (%) |
|---|---|---|---|---|---|---|---|---|---|---|
| 1 | 0–39.1 | −2.03 | 0.07 | 34 | 25 | 0.33 | 0.5 | 14 | 5.6 | 60 |
| 2 | 39.1–66.7 | −1.46 | 0.06 | 37 | 45 | 0.38 | 0.1 | 14 | 7 | 50 |
| 3 | 66.7–85.7 | −1.43 | 0.05 | 43 | 35 | 0.35 | 0.2 | 14 | 7 | 50 |
| *4 | 85.7–103.7 | −1.48 | 0.08 | 33 | 50 | 0.33 | 0.1 | 24 | 6 | 75 |
| 5 | 103.7–122.2 | −1.43 | 0.06 | 46 | 20 | 0.25 | 0.4 | 14 | 5.6 | 60 |
| 6 | 122.2–148.7 | −1.14 | 0.07 | 33 | 25 | 0.15 | 0.6 | 14 | 7 | 50 |
| 7 | 148.7–170.4 | −1.04 | 0.03 | 26 | 30 | 0.18 | 0.1 | 16 | 4.8 | 70 |
| 8 | 170.4–185.5 | −0.97 | 0.07 | 20 | 25 | 0.08 | 0.4 | 14 | 5.6 | 60 |
| *9 | 185.5–205.6 | −1.14 | 0.12 | 26 | 40 | 0.1 | 0.7 | 26 | 7.8 | 70 |
| 10 | 205.6–226.9 | −1.3 | 0.06 | 35 | 50 | 0.33 | 0 | 20 | 6 | 70 |
| 11 | 226.9–252.7 | −1.42 | 0.07 | 23 | 25 | 0.15 | 0.7 | 18 | 6.3 | 65 |
| 12 | 252.7–273.5 | −1.41 | 0.07 | 17 | 20 | 0.08 | 0.6 | 20 | 5 | 75 |
| 13 | 273.5–294.6 | −1.78 | 0.06 | 21 | 25 | 0.23 | 0.3 | 18 | 4.5 | 75 |
| 14 | 294.6–322.6 | −2.03 | 0.11 | 22 | 25 | 0.23 | 0.7 | 14 | 5.6 | 60 |
| 15 | 322.6–349.9 | −2.13 | 0.05 | 32 | 30 | 0.43 | 0.1 | 14 | 4.9 | 65 |
| 16 | 349.9–370.9 | −1.56 | 0.04 | 34 | 30 | 0.3 | 0.2 | 14 | 5.6 | 60 |
| 17 | 370.9–388.0 | −1.19 | 0.05 | 48 | 20 | 0.23 | 0.3 | 14 | 5.6 | 60 |
| 18 | 388.0–416.7 | −1.06 | 0.05 | 47 | 30 | 0.25 | 0.3 | 14 | 7.7 | 45 |
| 19 | 416.7–446.0 | −0.71 | 0.02 | 48 | 25 | 0.15 | 0.1 | 14 | 5.6 | 60 |
| *20 | 446.0–457.5 | −0.66 | 0.11 | 24 | 55 | 0 | 0.6 | 28 | 8.4 | 70 |
| 21 | 457.5–479.1 | −0.65 | 0.04 | 54 | 80 | 0.25 | 0 | 18 | 10.8 | 40 |
| 22 | 479.1–504.5 | −0.54 | 0.05 | 48 | 80 | 0.18 | 0.1 | 14 | 10.5 | 25 |
| 23 | 504.5–532.9 | −0.43 | 0.04 | 39 | 15 | 0.05 | 0.5 | 14 | 9.1 | 35 |
| 24 | 532.9–555.0 | −0.45 | 0.04 | 56 | 15 | 0.15 | 0.2 | 14 | 9.8 | 30 |
| 25 | 555.0–571.3 | −0.55 | 0.04 | 66 | 15 | 0.25 | 0 | 14 | 10.5 | 25 |
| 26 | 571.3–591.6 | −0.36 | 0.05 | 45 | 20 | 0.08 | 0.3 | 14 | 10.5 | 25 |
| 27 | 591.6–612.2 | −0.55 | 0.07 | 42 | 65 | 0.13 | 0.4 | 16 | 12 | 25 |
| 28 | 612.2–634.1 | −0.38 | 0.07 | 35 | 80 | 0.03 | 0.6 | 18 | 13.5 | 25 |
| 29 | 634.1–659.8 | −0.77 | 0.05 | 43 | 80 | 0.2 | 0.3 | 16 | 10.4 | 35 |
| *30 | 659.8–687.4 | −0.52 | 0.04 | 26 | 40 | 0.05 | 0.3 | 22 | 7.7 | 65 |
| 31 | 687.4–709.4 | −0.73 | 0.05 | 53 | 80 | 0.28 | 0 | 16 | 10.4 | 35 |
| 32 | 709.4–735.3 | −0.73 | 0.05 | 41 | 60 | 0.2 | 0.1 | 14 | 8.4 | 40 |
| 33 | 735.3–767.8 | −0.66 | 0.06 | 35 | 55 | 0.13 | 0.3 | 18 | 9 | 50 |
| *34 | 767.8–805.8 | −0.8 | 0.06 | 31 | 45 | 0.13 | 0.4 | 24 | 8.4 | 65 |
| *35 | 805.8–838.4 | −0.55 | 0.07 | 24 | 40 | 0.03 | 0.4 | 26 | 7.8 | 70 |
| 36 | 838.4–864.2 | −0.67 | 0.04 | 43 | 35 | 0.15 | 0.3 | 14 | 9.1 | 35 |
| 37 | 864.2–893.7 | −0.57 | 0.05 | 38 | 35 | 0.1 | 0.4 | 14 | 9.8 | 30 |
| *38 | 893.7–922.6 | −0.65 | 0.05 | 38 | 60 | 0.15 | 0.2 | 22 | 8.8 | 60 |
| *39 | 922.6–944.6 | −0.76 | 0.06 | 31 | 45 | 0.13 | 0.3 | 26 | 7.8 | 70 |
| *40 | 944.6–971.1 | −0.73 | 0.04 | 26 | 35 | 0.1 | 0.3 | 20 | 7 | 65 |

*Notes:* Symbol '*' represents data points with relatively poor constraints on key portions of the across-trench profile and thus were not plotted in Figs 6(c)–(i) and 7–10.

**Table C2.** Best-fitting bending parameters of the Mariana Trench.

| Section[*] | Along-trench distance (km) | $W_0$ (km) | $W_b$ (km) | $X_0$ (km) | $X_r$ (km) | $-V_0$ ($10^{12}$ N m$^{-1}$) | $M_0$ ($10^{17}$ N) | $T_e^M$ (km) | $T_e^m$ (km) | $T_e$ reduction (%) |
|---|---|---|---|---|---|---|---|---|---|---|
| 6 | 250.0–285.1 | −2.74 | 0.33 | 42 | 70 | −0.07 | 1.28 | 48 | 22.3 | 53.6 |
| 7 | 287.4–321.9 | −4.16 | 0.42 | 57 | 75 | 0.69 | 1.50 | 45 | 23.1 | 48.7 |
| 8 | 326.0–357.2 | −5.23 | 0.07 | 105 | 75 | 3.17 | 0.10 | 48 | 18.8 | 60.9 |
| 9 | 360.0–393.6 | −5.40 | 0.14 | 90 | 85 | 3.11 | 0.10 | 48 | 18.8 | 60.9 |
| 10 | 397.0–437.1 | −5.67 | 0.22 | 84 | 90 | 2.89 | 0.50 | 49 | 21.1 | 56.9 |
| 11 | 442.0–492.2 | −4.76 | 0.31 | 81 | 92 | 1.62 | 2.05 | 46 | 30.8 | 33.1 |
| 12 | 498.1–541.8 | −3.92 | 0.48 | 66 | 92 | 0.61 | 2.05 | 50 | 29.2 | 41.5 |
| 13 | 545.6–580.2 | −4.28 | 0.35 | 81 | 82 | 1.41 | 1.85 | 50 | 29.2 | 41.5 |
| 14 | 583.4–611.1 | −4.68 | 0.29 | 93 | 80 | 2.04 | 1.50 | 48 | 28.1 | 41.5 |
| 15 | 613.4–640.6 | −4.94 | 0.35 | 78 | 85 | 1.93 | 1.20 | 48 | 24.6 | 48.7 |
| 16 | 643.4–670.5 | −5.20 | 0.41 | 81 | 100 | 2.01 | 1.60 | 50 | 27.7 | 44.6 |
| 17 | 674.0–709.8 | −5.05 | 0.37 | 78 | 95 | 2.13 | 1.40 | 49 | 27.1 | 44.6 |
| 18 | 717.4–746.7 | −4.21 | 0.38 | 81 | 95 | 1.59 | 1.60 | 48 | 29.8 | 37.9 |
| 19 | 749.7–777.2 | −3.63 | 0.23 | 75 | 90 | 1.50 | 0.70 | 47 | 23.5 | 50.0 |
| 20 | 780.3–806.8 | −3.44 | 0.29 | 78 | 90 | 1.19 | 1.10 | 46 | 26.9 | 31.5 |
| 21 | 809.1–829.4 | −3.08 | 0.26 | 93 | 90 | 1.32 | 1.00 | 45 | 29.3 | 35.0 |
| 22 | 831.9–859.9 | −3.43 | 0.37 | 93 | 100 | 0.27 | 2.00 | 50 | 29.7 | 40.6 |
| 23 | 862.9–889.3 | −3.82 | 0.43 | 78 | 100 | 1.14 | 1.70 | 50 | 30.4 | 39.2 |
| 24 | 891.8–914.7 | −3.89 | 0.37 | 84 | 90 | 1.27 | 1.80 | 47 | 31.5 | 33.1 |
| 25 | 917.0–941.2 | −3.85 | 0.65 | 60 | 99 | 0.03 | 2.60 | 49 | 30.9 | 37.0 |
| 26 | 945.1–975.7 | −3.67 | 0.6 | 60 | 90 | −0.07 | 2.60 | 49 | 30.9 | 37.0 |
| 27 | 978.1–999.9 | −3.38 | 0.53 | 57 | 80 | −0.20 | 2.70 | 50 | 31.5 | 37.0 |
| 28 | 1002.3–1022.7 | −3.64 | 0.29 | 66 | 83 | 0.88 | 1.80 | 50 | 29.2 | 41.5 |
| 29 | 1024.9–1045.5 | −3.82 | 0.39 | 69 | 100 | 1.10 | 1.75 | 48 | 30.6 | 37.0 |
| 30 | 1047.8–1068.5 | −3.22 | 0.45 | 66 | 95 | 0.45 | 1.90 | 49 | 30.9 | 37.0 |
| 31 | 1070.8–1090.9 | −3.15 | 0.52 | 66 | 70 | −0.07 | 2.60 | 50 | 31.5 | 37.0 |
| 32 | 1093.1–1111.1 | −3.40 | 0.37 | 63 | 95 | 0.65 | 1.70 | 50 | 29.2 | 41.5 |
| 33 | 1115.3–1135.7 | −3.21 | 0.41 | 57 | 70 | 0.12 | 1.90 | 50 | 26.6 | 46.9 |
| 34 | 1138.1–1158.1 | −2.68 | 0.33 | 66 | 108 | 0.65 | 0.90 | 48 | 25.5 | 46.9 |
| 35 | 1160.3–1180.5 | −2.60 | 0.27 | 66 | 95 | 0.81 | 0.80 | 48 | 25.5 | 46.9 |
| 36 | 1182.7–1202.9 | −2.75 | 0.16 | 81 | 60 | 0.98 | 0.50 | 49 | 19.2 | 60.9 |
| 37 | 1205.3–1227.3 | −2.68 | 0.32 | 57 | 80 | 0.18 | 1.10 | 50 | 23.2 | 53.6 |
| 38 | 1229.6–1250.2 | −1.77 | 0.31 | 57 | 110 | −0.27 | 1.55 | 50 | 33.5 | 33.1 |
| 39 | 1252.6–1274.3 | −1.92 | 0.31 | 57 | 70 | −0.21 | 1.80 | 49 | 32.8 | 33.1 |
| 40 | 1276.8–1297.6 | −2.09 | 0.29 | 81 | 110 | 0.59 | 1.20 | 52 | 34.8 | 33.1 |
| 41 | 1300.0–1321.5 | −1.80 | 0.39 | 63 | 70 | −0.35 | 2.00 | 52 | 34.8 | 33.1 |
| 42 | 1323.9–1345.5 | −1.79 | 0.37 | 57 | 100 | −0.55 | 2.20 | 52 | 38.3 | 26.3 |
| 43 | 1347.8–1368.7 | −2.67 | 0.13 | 84 | 105 | 1.54 | 0.40 | 46 | 26.9 | 41.5 |
| 44 | 1371.1–1391.4 | −2.14 | 0.45 | 66 | 120 | −0.26 | 1.90 | 52 | 34.8 | 33.1 |
| 45 | 1393.8–1415.5 | −2.24 | 0.51 | 63 | 98 | −0.57 | 2.40 | 52 | 35.6 | 31.6 |
| 46 | 1417.8–1438.6 | −2.33 | 0.51 | 63 | 90 | −0.55 | 2.60 | 52 | 36.6 | 29.5 |
| 47 | 1441.3–1463.6 | −2.48 | 0.42 | 66 | 110 | 0.40 | 1.20 | 46 | 29.0 | 37.0 |
| 48 | 1465.9–1487.3 | −2.46 | 0.37 | 72 | 125 | 0.33 | 1.70 | 50 | 35.2 | 29.5 |
| 49 | 1490.0–1512.8 | −2.99 | 0.08 | 87 | 90 | 1.66 | 0.13 | 47 | 19.9 | 57.6 |
| 50 | 1515.5–1540.8 | −2.58 | 0.3 | 78 | 100 | 0.60 | 1.60 | 49 | 34.5 | 29.5 |
| 51 | 1543.0–1563.4 | −2.35 | 0.23 | 78 | 105 | 0.82 | 1.00 | 47 | 31.5 | 33.1 |
| 52 | 1565.8–1590.8 | −1.95 | 0.33 | 69 | 100 | −0.18 | 1.90 | 50 | 36.8 | 26.3 |
| 53 | 1599.3–1610.0 | −1.60 | 0.33 | 69 | 117 | −0.14 | 1.50 | 50 | 36.8 | 26.3 |
| 54 | 1618.5–1654.4 | −1.62 | 0.19 | 78 | 110 | 0.76 | 0.50 | 50 | 30.6 | 38.7 |
| 55 | 1656.7–1681.6 | −2.05 | 0.33 | 66 | 95 | 0.15 | 1.50 | 50 | 33.5 | 33.1 |
| 59 | 1763.6–1796.3 | −2.28 | 0.16 | 66 | 70 | 0.77 | 0.55 | 47 | 21.8 | 53.6 |
| 60 | 1798.7–1829.1 | −2.05 | 0.16 | 60 | 75 | 0.69 | 0.40 | 46 | 20.6 | 55.2 |
| 61 | 1832.0–1857.7 | −2.10 | 0.16 | 66 | 85 | 0.54 | 0.60 | 50 | 23.2 | 53.6 |
| 62 | 1860.5–1899.9 | −2.10 | 0.24 | 87 | 100 | 0.84 | 1.00 | 46 | 34.6 | 31.2 |
| 63 | 1902.3–1923.1 | −2.38 | 0.27 | 87 | 100 | 0.88 | 1.00 | 46 | 31.6 | 31.2 |
| 64 | 1925.7–1949.9 | −1.87 | 0.25 | 87 | 70 | 0.40 | 1.20 | 50 | 31.5 | 37.0 |
| 65 | 1952.8–1982.5 | −1.49 | 0.14 | 96 | 87 | 0.63 | 0.60 | 47 | 31.5 | 33.1 |
| 66 | 1984.9–2010.9 | −1.57 | 0.23 | 87 | 110 | 0.32 | 1.10 | 50 | 36.8 | 26.3 |
| 67 | 2013.2–2044.7 | −1.39 | 0.35 | 60 | 80 | −0.59 | 2.00 | 50 | 39.7 | 20.6 |
| 68 | 2061.7–2138.6 | −1.91 | 0.28 | 72 | 90 | 0.10 | 1.60 | 49 | 36.1 | 26.3 |
| 69 | 2142.6–2179.2 | −2.20 | 0.18 | 78 | 83 | 0.70 | 1.00 | 49 | 29.8 | 39.2 |
| 70 | 2191.8–2209.3 | −1.53 | 0.31 | 60 | 90 | −0.30 | 1.60 | 49 | 36.1 | 26.3 |
| 71 | 2212.5–2328.9 | −0.87 | 0.33 | 51 | 90 | −0.73 | 1.48 | 48 | 38.1 | 20.6 |

[*]*Note:* Sections that are relatively poorly constrained, including the Sections 1–5, 56–58 and 71–75, are not shown in this study.